Final Technical Report

USGS Grant G18AP00062

On the Variability of Earthquake Ground Motion from the Sage Brush Flats High Density Array

Deborah L. Kilb[1]

1. Scripps Institution of Oceanography, University of California San Diego, La Jolla, CA, USA

Note: This work was completed in collaboration with Christopher W. Johnson, Annemarie Baltay and Frank Vernon

Key points:

1. Data from a dense seismic array (>1000 nodes; 0.6x0.6 km^2) shows spatial variability in peak ground velocity of 20-37% of the mean.

2. Higher ground motions are produced within the small basin structure, and lower ground motions are produced within the fault zone.

3. Surface recordings of 38 select earthquakes (2≤M≤4.2) produce peak ground velocities that are 3-10 times higher than recorded at a 148 m deep borehole sensor.

Abstract

We explore the spatial variability in peak ground velocity (PGV) at Sage Brush Flats (SGB) along the San Jacinto Fault in southern California. The SGB dense array spans a 0.6x0.6 km^2 footprint and includes 1,108 geophones deployed for ~1-month in 2014 (07 May through 13 June), with station spacings 10m - 30m. We focus on 38 ($2 \leq M_L \leq 4.2$) events within 200 km of the network. The faults and small basin in the region have a significant impact on PGV, producing PGV variations ranging up to 20-37% of the mean. The surface PGV measurements exceed a co-located borehole station (depth 148 m) PGVs by factors of 3-10, confirming that local fault structure, basins, topography and amplification from surface soft sediments increase PGVs. Within the basin, we find high PGVs regardless of the azimuthal trajectory of the seismic waves across the array. A co-located pair of $M_L 2.6$ events produce repeatable PGV values of 0.00170 ± 0.00042 and 0.00145 ± 0.00034 cm/s and show similarities in their spatial PGV patterns. The average corner frequencies of these two events are similar (~11-16 hz), but the viable measurements of stress drop are large at ~6MPa. We also find that rupture directivity can increase the PGVs by 167%. We conclude that similar earthquakes produce repeatable ground motions, and the PGV values are variable across the array, suggesting spatial extrapolation of PGV values in regions of known faults and basins, even across a small footprint, should be done with caution.

Keywords: peak ground velocity, dense nodal array, San Jacinto Fault Zone, California, ground motions, GMPE, PGV, PGA, directivity, repeatability, earthquake

1. Introduction

Ground-motion modeling is a key component to earthquake hazard mapping and risk reduction. How seismic energy from an earthquake source attenuates as seismic waves travel from the source to the recording stations is an integral part of ground motion modeling and prediction equations, and has been of great interest to seismologists for decades (*e.g.,*Press, 1964; Anderson, 1986; Hough *et al.*, 1988; Abercrombie, 1995; Aki and Richards, 2002; Anderson, 2007; Atkinson *et al.*, 2007; McNamara*et al.*, 2014; Yabe *et al.*, 2014; Baltay and Boatwright, 2015; Zigone *et al.*, 2015; Bostock *et al.*, 2017; Wang, 2019). Seismic waves do not propagate uniformly in all directions (Kilb *et al.*, 2000; Ammon *et al.*, 2011; Denolle *et al.*, 2014; Gallovic, 2016), which can result in significant variability in the ground motions at sites the same distance from the mainshock that are located within different geologic structures (Hanks, 1975). In addition to the attenuation of seismic waves with distance, it is also important to understand how the amplitude can be altered by basin geometry, fault zone guided waves, material heterogeneities, rupture directivity, or a combination of these and other effects.

As ground-motion prediction equations (GMPEs) move towards source-path-site specific models (i.e., non-ergodic, or spatially varying coefficients, i.e., Landwehr et al., 2016), we need to better understand both the observed variability in ground motion at any one site, and the spatial correlation pattern of ground motion within small regions. By improving our uncertainty models, we can in turn improve the accuracy of hazard maps (Bommer and Abrahamson, 2006; Baltay and Hanks, 2014; Baltay *et al.*2017; Ghofranii et al., 2019). The Sage Brush flats array, with

~1000 sensors in an area of ~0.36km^2 yielding station spacing of 10-30m, and high-seismicity rates, is an ideal location at which to study the spatial variability and patterns in ground motion.

In this study, we examine variability in ground motion using data from the Sage Bruch Flats (SBF) 30-day dense geophone deployment in southern California. We focus on peak ground velocity (PGV) and for completeness we include peak ground acceleration (PGA) results in the electronic supplement. The SBF array configuration allows detailed analysis of local site effects that alter the ground motions on length scales less than a kilometer. To assess the similarities and differences, we explore a pair of co-located events and a pair of earthquakes of similar magnitude but different arrival azimuth. We quantify the variability in ground motion within the array footprint and evaluate differences observed for events at different distances and magnitudes. The characteristics of ground motions presented herein provide additional quantification of the systematic uncertainty in GMPE used to produce hazard maps, and will help inform how to reduce uncertainty to improve GMPEs used in seismic hazard estimates for southern California.

2. Data and Method

2.1 Seismic Network Deployment and data recording

Our study area is Sage Brush Flats (SGB) along the Clark strand of the San Jacinto fault zone (SJFZ) in southern California (Figure 1). A dense array of 1,108 Fairfield 10 Hz vertical component geophones, referred to as nodes, were deployed in a 0.6 km by 0.6 km area from 07 May 2014 through 13 June 2014 (~1 month) recording at 500 Hz (Ben-Zion *et al*., 2015). The layout consists of a grid with 20 rows spaced about 30 m along the fault containing 50 nodes perpendicular to the fault at a nominal 10-meter spacing. An additional 108 sensors were deployed as extensions to multiple rows. The location of each sensor was surveyed using a Real Time Kinematic GPS system to an accuracy of approximately 30 cm. This array was co-located with a borehole seismometer, B946, at a depth of 148 m. The spatial extent of the array footprint contains a local basin extending about 200 m west of the fault and is bounded by hillslopes up to 70 m containing granitic boulders to the east and west.

The ANZA seismic network recorded >900 local earthquakes within 200 km of SGB during the 30-day deployment. The arrival times for these events were manually reviewed and a catalog with locations and magnitudes was compiled. We augment this catalog with regional M≥2 events within 200 km of the array from the Southern California Seismic Network (SCSN) catalog, with the largest event a M4.1 earthquake 186 km from the array. The ANZA catalog magnitudes were derived using the Antelope *dbml* algorithm, which differs from the algorithm used to compute the SCSN magnitudes. Using spatiotemporal matching we identify earthquakes in both catalogs and select the SCSN magnitude for all matching events. For the ground motion analysis, we select the 38 M≥2 earthquakes that have a cataloged arrival time at the borehole sensor and was recorded by >1000 nodes. The borehole sensor p-wave and s-wave hand-picked arrival times provide a constraint for the time window of interest at the array. The waveforms of each node are analyzed to quantify the spatial heterogeneity of PGV and PGA of the seismic waves.
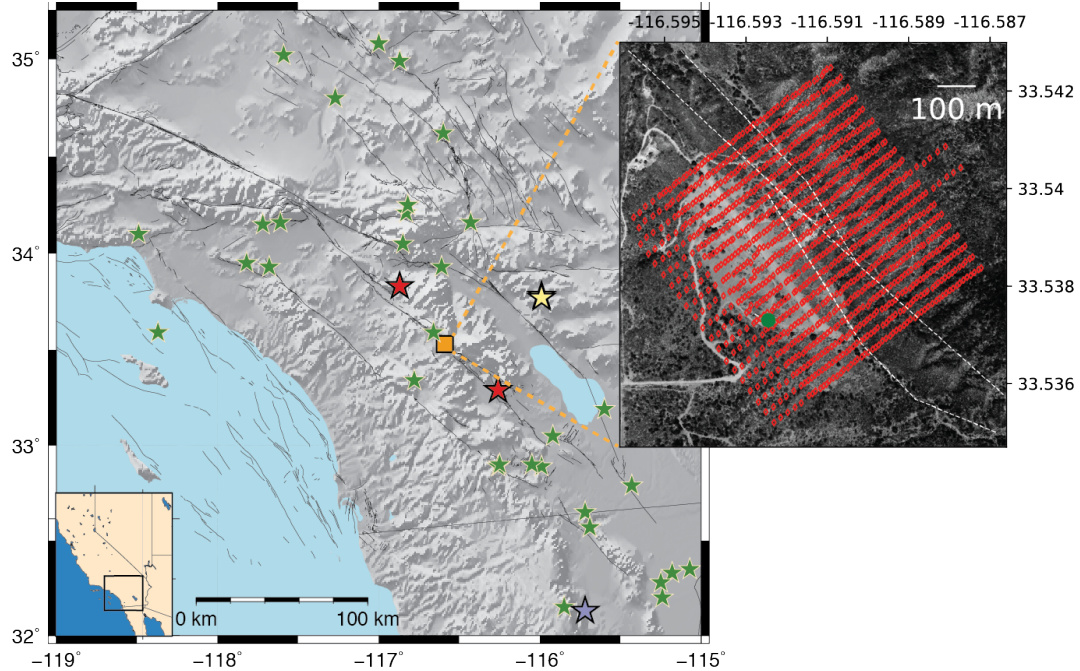
Figure 1. Earthquake locations (stars) of the select 38 M≥2 events within 200 km of Sage Brush Flats (orange square; -116.59, 33.54) when a large portion of the array was recording (N stations ≥1000). Black lines are the regional fault locations from the USGS database. Key earthquakes include a pair of repeat events (yellow overlapping stars), two Baja events that temporarily overprint each other who's origin times differ by 1 second and produce high amplitudes in the eastern portion of the array (blue stars), and two events at similar source-station distances but different azimuths (red stars). The remaining events are shown as green stars. (Inset) Locations of the geophone array containing 1,108 sensors (red diamonds). The San Jacinto Fault strands (white dashed lines) and the location of the borehole seismometer B946 (green dot) are also shown.

2.2 Data processing and data selection

For each $M_L \geq 2$ earthquake the >1,000 nodal waveforms are extracted in 30 sec segments beginning 1 sec before the p-wave arrival time. The waveforms are detrended and a 5% cosine taper is applied before deconvolving the instrument response function to obtain velocity data in units of m/s. Acceleration records are calculated by taking the derivative of the velocity. The waveforms are bandpass filtered with corners of 4 and 40 Hz. The high frequency filter corner was selected to avoid instrumental noise around 40Hz (Farrell et al., 2018; Johnson et al., 2019a) and the low filter corner was selected to avoid numerical artifacts below the 10 Hz instrumental corner frequency. The signal-to-noise ratio (SNR) of each trace is calculated using 1 sec of data before and after the p-wave arrival. The absolute PGV and PGA values are calculated using the maximum for the entire 30 second record. Amplitude spectra are computed using the Fourier coefficients of the first 10 seconds of the unfiltered s-wave velocity waveforms. The results are organized in a Python data frame to allow easy parameter filtering and event selection (Table S1).

We use the full suite of 38 $M_L \geq 2$ earthquakes (Table 1) to examine the overall site behavior and select a subset of 5 key earthquakes to examine the ground motion relationship between

magnitude, distance, and back-azimuth (Figure 2). The key earthquakes highlighted in Figures 1 and 2 include: (1) a pair of repeating events (yellow stars), (2) events with similar magnitudes, depths and distances, but near opposite back azimuths (red stars), and (3) an event doublet in Baja that produce large p-wave amplitudes and higher PGVs in the eastern part of the study region.
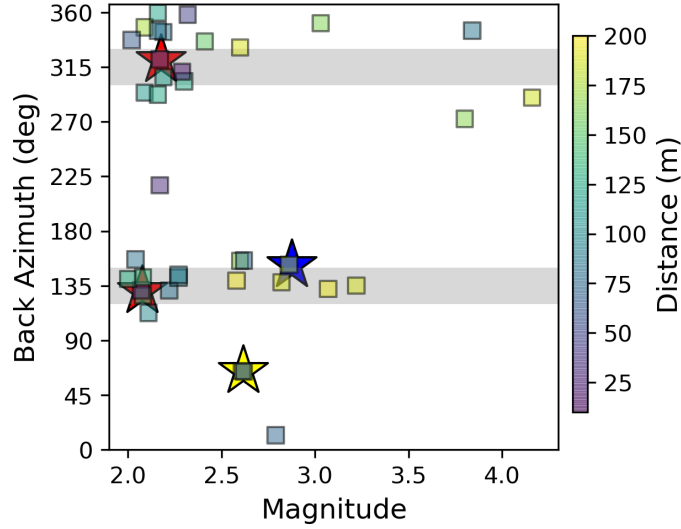

Figure 2. Magnitude and back azimuth of select 38 2≤M_L≤4.2 earthquakes (square symbol colored by distance). Gray bars indicate back azimuths that locate along fault. The stars indicate key events, where the color scheme is the same as that in Figure 1.

3. Results

3.1.1 PGV as a function of distance and magnitude

The relationship between PGV and distance and magnitude for the 38 key events is consistent with the GMPE of Abrahamson et al., 2014 (Figure 3). When processing, we first remove waveforms that have a SNR≤1.5 and outliers are removed by applying the fence method to the suite of PGV values obtained for each event (Appendix A). The PGV as a function of distance results show the range of values for each event and indicate a decaying log-log relationship (Figure 3a). Two events produce the highest PGV values include the nearest earthquake, a M_L2.3 at 19 km, with a median PGV of 0.0124 cm/s and 24% variability from the mean. The second largest PGVs are produced by a M_L3.8 event at 83 km with a median PGV of 0.0112 cm/s and 26% variability. Both events show PGAs exceeding 1.0 cm/s^2 at some locations in the study area (Figure S1). The largest event is a M_L4.2 with a median PGV of 0.00054 cm/sec and 40% variability. The PGA for this event is 0.02457 cm/s^2. The lower PGV from the M_L4.2 scales with the relatively large distance of 186 km from the array. The PGV as a function of magnitude shows a trend of increasing PGV that decreases with distance (Figure 3b). The range of ground motions do not indicate any clear outlier events, but some do show a larger variability in PGVs across the array.
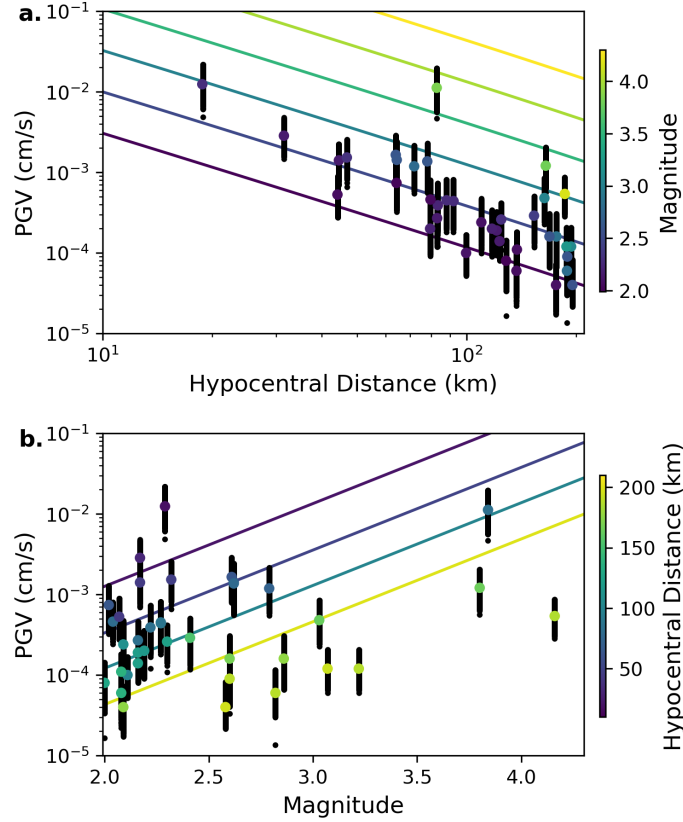
Figure 3. PGV for the 38 select events ($2 \leq M_L \leq 4.2$) recorded by at least 1000 nodes (black dots) as a function of (**a**) hypocentral distance with the median value colored by magnitude and (**b**) magnitude with the median value colored by distance. Both plots include the expected ground motions predicted by the GMPEs of Abrahamson et al., 2014 (solid lines). A similar figure of PGA is included in the electronic supplement to this manuscript (Figure S1).

3.1.2 PGV vs PGA

The SGB array is co-located with borehole station B946 (depth 148 m). We find the PGVs recorded at the surface are a factor of 3-10 higher than the borehole measurements (Figure 4a). These scale factors are on par with the scale factor of ~4 found in the work of Baltay et al., 2013, which examined data from a ~100 m borehole and surface recordings of 59 earthquakes in eastern Honshu, Japan. When we further partition the data by frequency, we find that the higher frequency data show smaller scale factors, which is consistent with these frequencies being above the PGV corner frequencies and therefore they will be reduced in amplitude (Figure 4b).
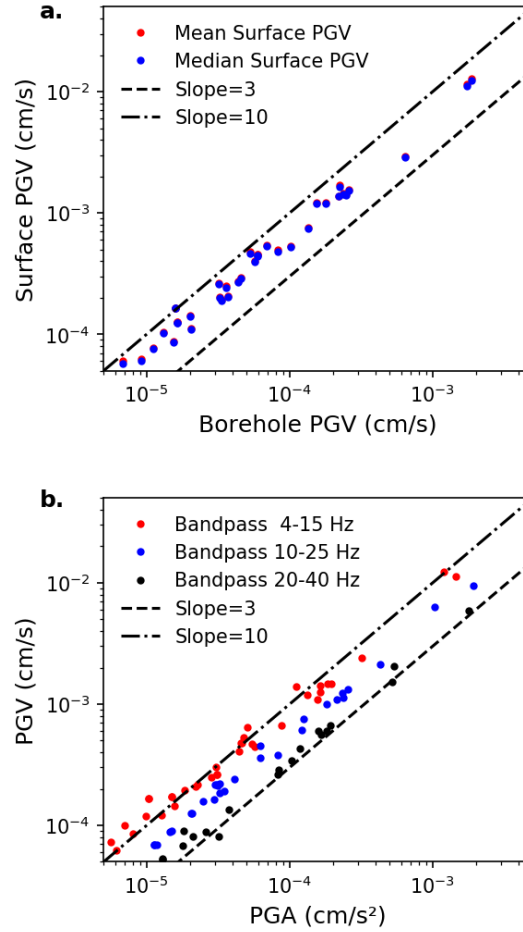
Figure 4. Comparison of PGA and PGV values from data from all nodes that recorded our select 38 events. (**a**) Comparison of PGV recorded at the borehole station B946 (depth 148 m) with the median and mean surface PGV values derived after removing outliers. Similar plots for PGA values can be found in supplemental information (Figure S2). (**b**) PGV vs. PGA for different frequency ranges.

3.2 Ground motion repeatability

Ground motion repeatability is explored using two $M_L 2.6$ events on 14 May 2014 at 07:45:39 and 08:03:22 located within 0.5 km of each other. These earthquakes are separated by 18 minutes and are located 62 km from the array with a back azimuth of 64°. The mean PGVs with 1-standard deviation are 0.00145±0.00034 and 0.00170±0.00042 cm/s with a maximum of 0.00287 and 0.00242 cm/s, respectively (Figure 5). The surface recorded median PGV amplitudes across the array increase by a factor of 7.6 and 6.1, respectively, when compared to the borehole PGVs. The positive skew (see Appendix B) of 0.4 and 0.3 suggests some areas in the array experience higher ground motions, and indeed the spatial distribution of PGVs highlights locations with increased ground motions outside of the fault (Supp. Figure S3). Both events produce low amplitudes within the fault zone, and high amplitudes in the basin southwest of the fault and along the hillslope east of the fault. Comparing the PGVs from each node shows the ground motions are equivalent within 0.001 cm/s with a mean residual of 0.00023 cm/s

(Figure 6). The positive residual mean value is produced by slightly higher ground motions from the first $M_L 2.6$ event, but no particular area shows a concentration of higher velocities.
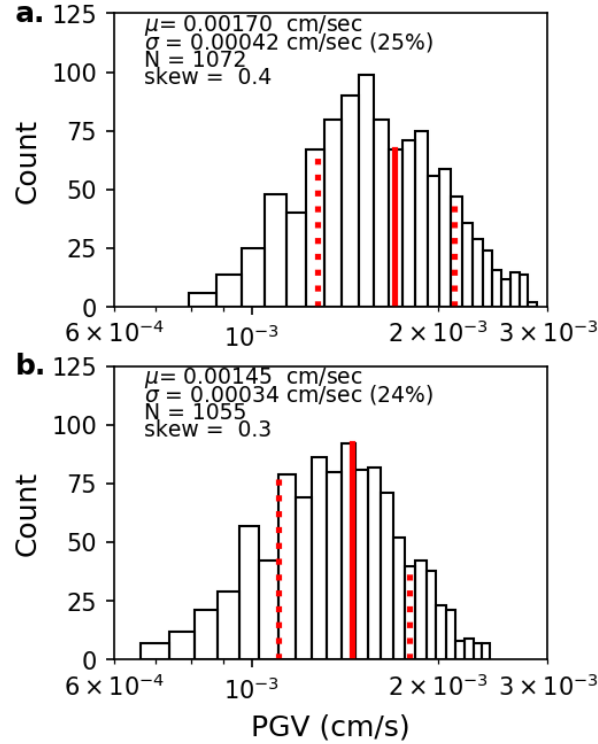
Figure 5. PGV distributions for a pair of repeating $M_L 2.6$ events on 14 May 2014 at (**a**) 07:45:39.09 and (**b**) 08:03:22.79. Metadata of the distribution mean (solid red line, μ), 1-standard deviation (dashed red lines, σ) with the ratio of the mean and standard deviation as a percentage in parentheses, number of nodes (N), and skewness (skew, see Appendix B) is included within each subplot.
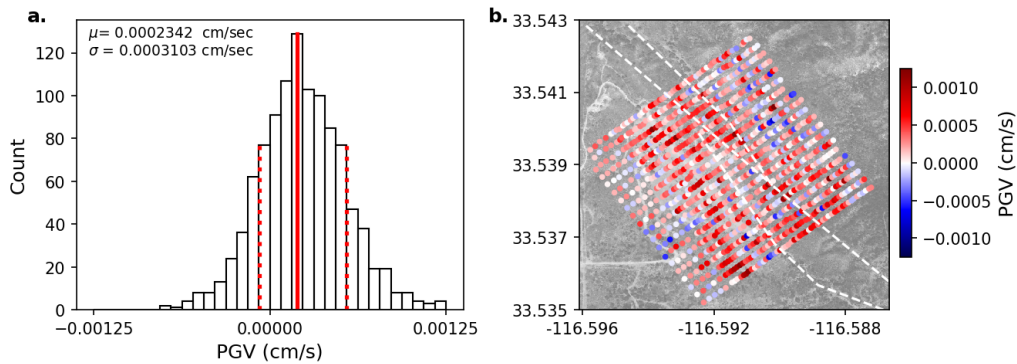
Figure 6. Comparison of the PGVs from the pair of $M_L 2.6$ events on 15 May 2014. (**a**) Distribution of PGV residuals. (**b**) Residual map of the difference in PGV values for each node.

3.3 Ground motions from along fault earthquakes

We next examine two events that have similar magnitudes ($M_L2.2$ and $M_L2.1$), depths (17 km), and distances from the network (41 km), but have different along-fault back azimuths (132˚ and 320˚). The $M_L2.2$ is along fault to the southeast and produces a mean PGV of 0.00144 cm/s and the $M_L2.1$ is along fault to the northwest and produces a mean PGV 167% smaller at 0.00054 cm/s (Figure 7). Both events show variability of 21-23% and a skew of 0.3 and 0.4, indicating the ground motion response is similar, but the PGVs are substantially smaller for the southeast event. We attribute these differences to rupture directivity effects. The PGV spatial patterns, however, are similar with the same higher ground motions in the basin and eastern hillslope, and lower PGV's within the fault proper (Figure 8).

Figure 7. PGV distribution produced by two similar sized along-fault events both located approximately 41km from the network (red stars in Figure 1). (**a**) $M_L2.2$ on 19 May 2014 17:07:05 with a back azimuth of 132˚ and (**b**) $M_L2.1$ on 24 May 2014 23:52:26 with a back azimuth of 320˚. Additional metadata is as in Figure 5.
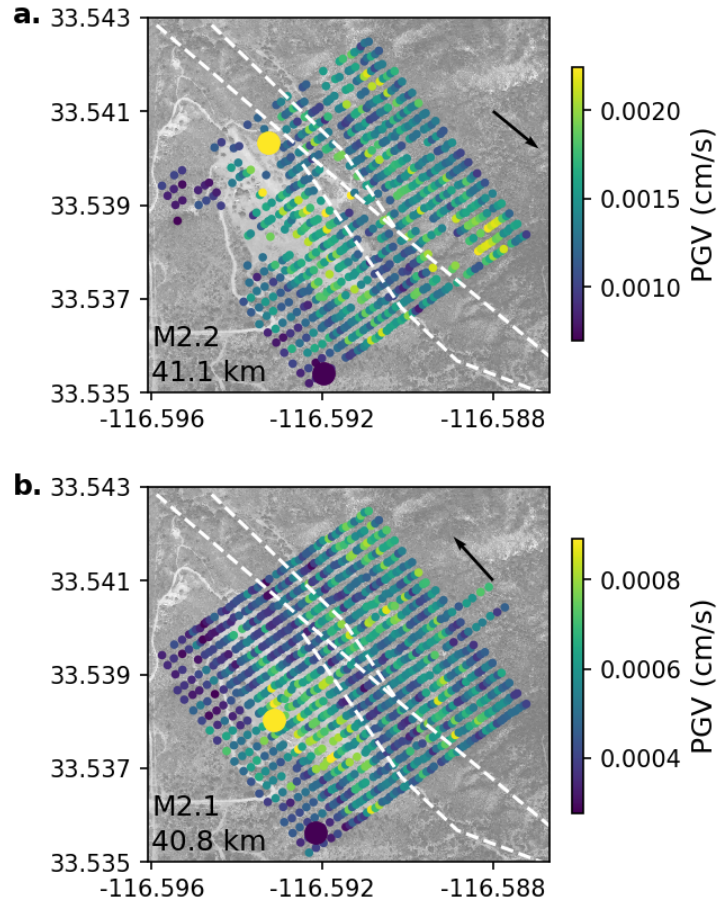
Figure 8. Map of PGV values from the two along-fault events shown in Figures 5-6. (**a**) $M_L 2.2$ on 19 May 2014 17:07:05 wit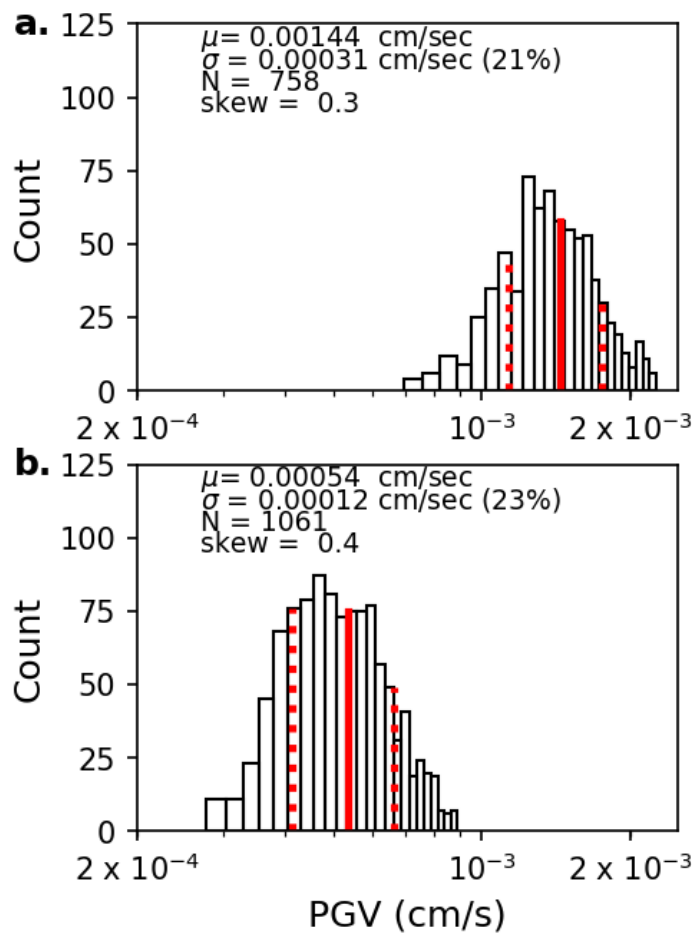h a back azimuth of 132˚, and (**b**) $M_L 2.1$ on 24 May 2014 23:52:26 with a back azimuth of 320˚. White dashed lines map the fault and black arrow indicates the orientation of the back azimuth, where the arrow points in the direction of the event. Large dots show the PGV minimum (dark blue) and maximum (yellow) locations within the array. Some of the nodes are missing in (a) because these data were removed when the fence was applied.

3.4 Baja doublet events produce high ground motions in the east

We next explore an earthquake doublet in Baja that temporally overprint each other as their origin times are 1-second apart (blue stars in Figure 1). These events occurred on 26 May 2014 with a $M_L 2.9$ at 12:16:07 followed by a $M_L 2.6$ at 12:16:08. In general, we can divide our suite of 38 events into three categories, where the PGVs are dominated by: (1) the s-waves, (2) the p-waves or (3) a combination of both. Typically, PGVs from along-fault events are dominated by s-waves (category 1). Notably, the Baja doublet produces relatively large P-wave amplitudes, which dominate the PGV valves. Unlike the along-fault events that produce large ground motions primarily in the basin structure, this doublet produces large ground motions on the eastern side of the fault (Figure 9).
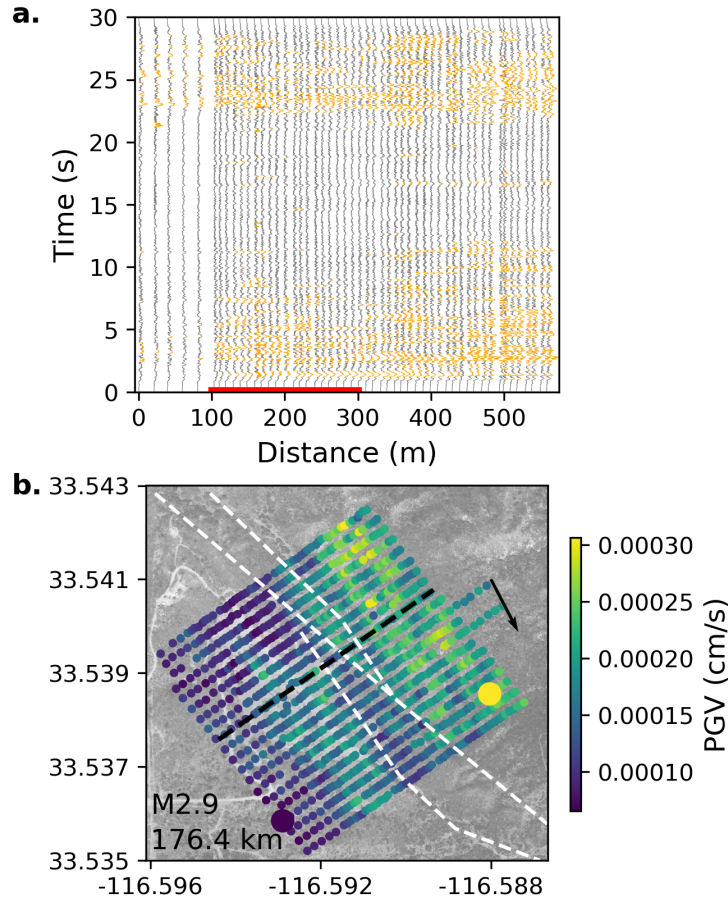
Figure 9. Data from the May 26th Baja event doublet (N=1070) at 176.4 km that produced large ground motions on the eastern side of the fault. (**a**) Waveform envelopes along the transect shown by the black dashed line in (**b**). The x-axis is the distance from the most western node and the y-axis is time in seconds starting 1 second prior to the p-wave arrival. The basin location is depicted with a red horizontal line along the x-axis. The waveforms are orange when the envelope amplitude exceeds twice the average of all record sections. Note the large p-wave signal. (**b**) Mapped PGV values show large amplitudes on the eastern side of the fault (white dashed lines). The black arrow is the back-azimuth orientation.

3.5 Velocity structure of the upper ~150 m

We next leverage borehole (148 m depth) and surface recordings of >1000 handpicked p-wave arrivals (identified using the borehole data) to more precisely understand the velocity structure within the upper ~150 m in this region using a borehole to surface time lag metric. For each earthquake a 5-20 Hz bandpass filter is applied to the borehole and surface station waveforms and a 5 second wavelet is selected starting 1 second before the P-wave arrival. Each surface waveform is downsampled to 100 Hz and cross-correlated with the borehole record. All records with a correlation coefficient >0.7 are used to estimate the median positive time lag for each station. We assume any sub-vertical incident angles of nearby events are not biasing the results. We account for variation in topography using the surface station elevation measurements that are relative to the borehole depth and known within 30 cm from the Real-Time-Kinematic GPS survey performed during installation. This procedure is repeated using the s-wave arrival times.

To highlight the variability of the p- and s-wave velocity structure between the borehole and the surface stations, the results are shown as the percent change from the median velocity of each (Figure 10). We find the slowest travel times are along the fault strands with a decrease up to 40% for both P-waves and S-waves. East of the fault zone we find a ~20% increase in P-wave velocity and ~35% increase in S-wave velocity. The hillslopes west of the fault indicate a 50% increase in P-wave velocity.
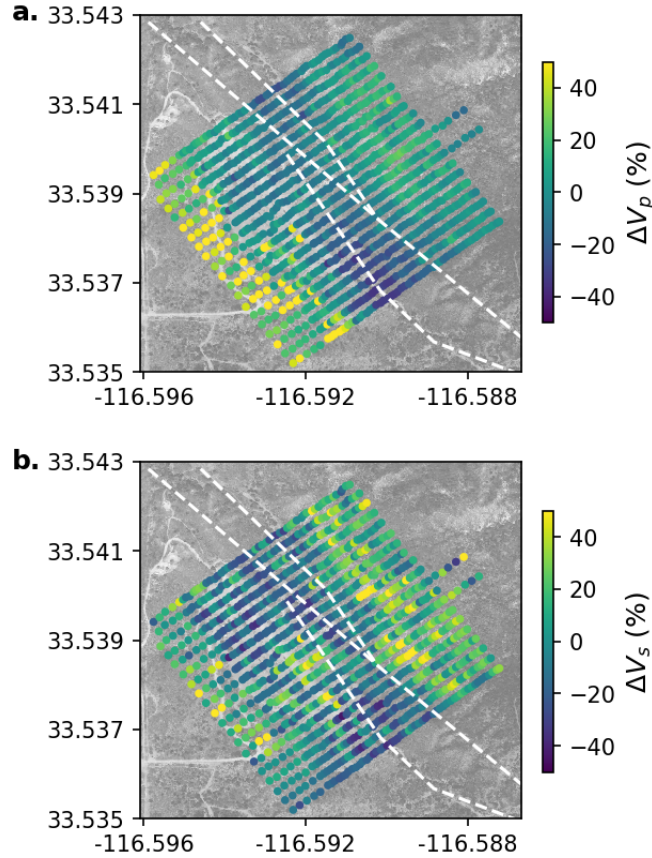
Figure 10. Comparison of borehole and surface recordings. Percent difference in (**a**) P-wave and (**b**) S-wave velocity within the top ~150 m of our study region. These values were derived using travel time difference between the borehole and the surface data, and then comparing these differences to the collective median.

3.6 Seismic moment, corner frequency, and stress drop

We next explore the variability of the corner frequency and stress drop across the network for the repeating pair of $M_L 2.6$ events discussed in section 3.2 above. As there is a known trade-off between corner frequency and seismic moment (M_0) estimates (Hiramatsu et al., 2002; Wang, 2019), we use the method of Kilb et al. (2012) to determine the optimal corner frequency, M_0 and kappa values that minimize the model misfit to the data without any *a priori* assumptions, in this way we solve for M_0, f_c, and kappa using only the spectral shape. We test a wide range of corner frequencies 1-40 Hz at increments of 0.1 Hz and apply this method to all viable waveforms (i.e., after applying the SNR; no fence was applied), tracking the favored M_0 and corner frequencies for each spectra from each node (>1,000 values for each quake). We only retain values that have a well constrained corner frequency between 5-20 Hz and a kappa value

>10 ms. For each event, we use the mean and standard deviation of these results to represent the final M_0 and corner frequencies, and their associated uncertainties (Figure 11). The fall-off of the spectra beyond the corner frequency, represented by the kappa value, is also computed. However, these earthquakes fall in the magnitude range $1 \leq M_L \leq 3.5$ where kappa values are not considered robust because the corner frequencies are within the center of the frequency span of interest, thereby not allowing the frequency-fall off (kappa) to be adequately estimated (Kilb et al., 2012). These kappa values should not be over interpreted and represent only an approximate value. With this caveat, we find the kappa values are relatively high at 26.43±5.88 and 30.69±6.59 ms for the first and second event, respectively, which is consistent with past studies analyzing data from this region (Kilb et al., 2012; Klimasewski, et al., 2019).
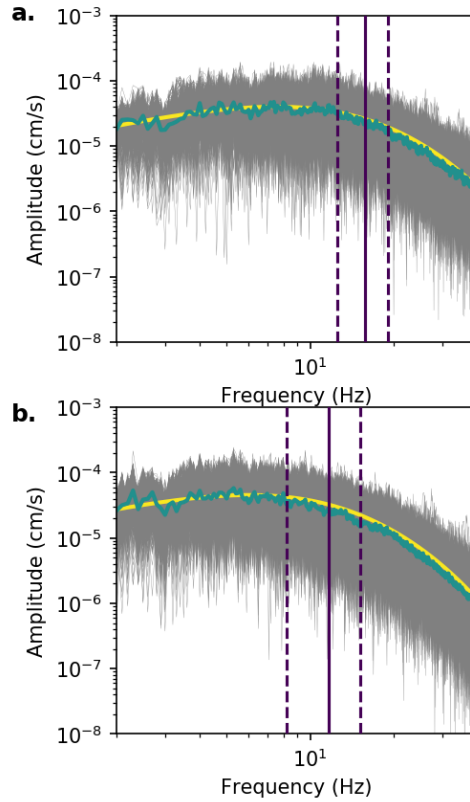
Figure 11. Spectra (gray curves) that have a well-defined corner frequency for the $M_L 2.6$ events on 14 May 2014 at (**a**) 07:45:39.09 (f_c=15.77±3.24 Hz; N=414) and (**b**) 08:03:22.79 (f_c=11.70±3.48 Hz; N=810). The average corner frequency is shown by the vertical purple line with one standard deviation shown with dashed lines. In green are all the median spectral amplitude and in yellow is the model using the average corner frequency, kappa value, and M_0 . The x-axis and y-axis scales are the same, which helps to highlight the similarity in the corner frequency and Mo estimates.

We next compute earthquake stress drops for both events, using equation 1 that assumes circular faulting (Brune, 1970, 1971; Berenev, 2001), where f_c is the corner frequency, and β is the shear wave velocity of 3.5 km/s at the source.

$$\Delta\sigma = \frac{7 \cdot M_0}{16} \left(\frac{2 \cdot \pi \cdot f_c}{2.34 \cdot \beta} \right)^3 \qquad (1)$$

In this equation there is no source-station distance parameter and the stressdrop is dependent on the cube of the corner frequency. We find the spectral characteristics of the two $M_L2.6$ events are similar (Table 3). The derived terms f_c, $\Delta\sigma$, $\log_{10}(Mo)$, and kappa produce similar average results within the uncertainties for the two events. For the two sets of waveforms associated with each event we find uncertainties in the corner frequency of ~3-4 Hz and uncertainties in stress drop of ~1-2 MPa (Figure 12). However, that finding relies on 100's of measurements for each event at the same location, which allows a mean and standard deviation to be determined using the full range of results from the viable spectra. Without a suite of measurements within a small spatial footprint we would not be able to discern the site-specific favored parameter values. If instead we assume each node is a stand-alone measurement, the conclusion would be that for all data that have a well constrained corner frequency the associated stress drop would span a range of 6 MPa.

Table 3. Spectral analysis results from the pair of repeating $M_L2.6$ earthquakes on 14 May 2014. Event #1 and #2 correspond to the first and second earthquake, respectively. The mean and standard deviations were derived using only results that had well constrained corner frequencies and the full viable range is the extent of the values.

Parameter	Event #	Number of viable nodes	Full viable range	Mean with 1 standard deviation
f_c	1	414	3-20 Hz	15.8±3.2 Hz
f_c	2	810	5-20 Hz	11.7±3.5 Hz
$\Delta\sigma$	1	414	0-6 MPa	1.9±1.2 MPa
$\Delta\sigma$	2	810	0-6 MPa	1.2±1.1 MPa
log(M0)	1	414	12.0-12.6 N-m	12.3±0.1 N-m
log(M0)	2	810	12.1-12.7 N-m	12.5±0.1 N-m
kappa	1	414	10-38 ms	26.4±5.9 ms
kappa	2	810	10-53 ms	30.7±6.6 ms
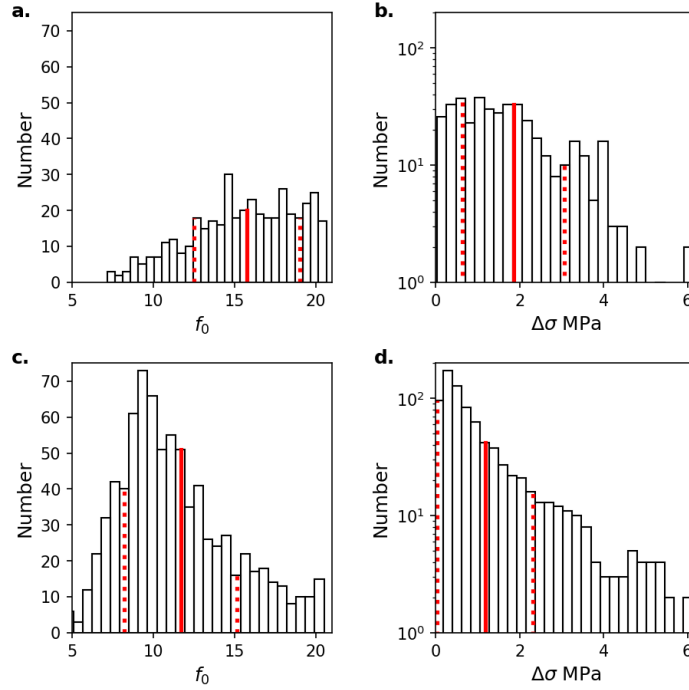
Figure 12. Distributions of modeled corner frequency and stress drop for a pair of repeating $M_L2.6$ events on 14 May 2014 at (**a** and **b**, n=414) 07:45:39.09 and (**c** and **d**, N=810) 08:03:22.79. Solid red line is the average and dashed lines are 1 standard deviation. There are fewer measurements for the first event because many of the spectra did not have a well-defined corner frequency.

4. Discussion

As expected, we find ground motions produced by an earthquake do not decay uniformly with source-station distance (Hanks, 1975) and instead find irregularities in the fall-off rates to be particularly dictated by the fault itself and the local basin structure on the west side of the Clark Fault. This basin structure is prone to systematically producing higher PGVs, regardless of the traversal of the seismic waves across the network. In comparison, this small basin structure pales in size with, for example, the Los Angeles, California, basin that is orders of magnitude larger and made up of marine and fluvial sediment that can be as thick as 10 km (Hauksson 1990; Liu et al, 2018). This suggests that the 19±31% variability in PGV across our small aperture array is likely much smaller than the scaling we might observed in the Los Angeles basin following a large earthquake.

Stress drop characterizes the earthquake source process during faulting through ground motion observations. Two primary methods to compute stress drop include the Brune (1970, 1971) method (Equation 1 above) and a spectral ratio method that uses a smaller earthquake with similar location as an Empirical Green's Functions (i.e., Baltay et al., 2013; Huang et al., 2016; Yoshimitsu et al., 2019). After five decades there is still currently no consensus if stress drop scales with magnitude or with other parameters such as faulting type, depth, etc. (King and Knopoff, 1968; Hanks and McGuire, 1981; Abercrombie & Leary, 1993; Ide & Beroza, 2001; Goebel et al., 2018). The Brune methodology requires a very accurate measure of the spectral

corner frequency and assumes the stress drop is not a function of magnitude. This approach represents a constant stress drop value scaled by distance. On the other hand, the spectral ratio method requires a sufficiently similar pair of earthquakes at the same location where one is substantially smaller than the other. The requirements for each approach can be difficult to obtain, making it challenging to ascertain if any observed variability in the results should be attributed to earthquake source properties or to incorrect model assumptions.

We show how measurements of corner frequencies and stress drop deviate within our spatially small study region. For the pair of repeating M_L2.6 events we find corner frequencies of 11-16 Hz, and stress drops of 1.2-1.9. These stress drops are comparable to those of Shearer et al. (2006) that found stress drops of small earthquakes ($1.5 \leq M_L \leq 3.10$) along the SJFZ on the order of 1.0 - 2.5 MPa. We find corner frequency and stress drop deviations of 1-2 Hz and 1-2 MPa, respectively, which are relatively small but require 100s of measurements at the same location. The ~6 MPa span in stress drop and 20hz span in corner frequency is consistent with other studies of small magnitude earthquakes that also caution that three can be significant uncertainties in these estimates (Abercrombie et al., 2017). These ranges represent the variability at one station location with a single back azimuth, in the traditional sense, so deviations typically attributed to recordings at different back-azimuthal variations do not apply here.

5. Conclusions

In this work, we investigate data recorded by the SGB vertical component seismic network (0.6 km by 0.6 km; 1088 stations when fully operational), focusing on 38 events ($2 \leq M_L \leq 4.2$) within 200 km of the network centroid. Consistent with the results of Ben-Zion *et al.*, (2015) we find that the ground motions recorded across the SGB array from an individual earthquake are not uniform, typically producing higher ground motions within the basin structures on the southwest side of the Clark fault and lower ground motions within the fault zone. We find two co-located M_L2.6 events (yellow stars in Figure 1) produce similar PGV values and PGV spatial patterns across the network within the assumed uncertainties. This suggests that although the deviations in ground motions across the network are relatively large, the mapped spatial patterns from co-located events produce similar results.

We find directivity effects play a strong role in PGV values, having the ability to alter the PGV values by 167%. This was determined by examining two along-fault events that were both 41 km from the array, but their back-azimuths differ by 188° (compare 132° and 320°; red stars in Figure 1). These two events have similar magnitudes (M_L2.2 and M_L2.1) and both were at a depth of 17 km, given these similarities we attribute large differences in PGVs to directivity effects.

An additional finding is from an earthquake doublet on May 26th Baja (M_L2.9 and M_L2.6; overprinted blue stars in Figure 1) that occurred within one second of each other. This doublet produced large P-wave signals across the network, strongly amplifying the regions on the eastern side of the fault. This differs from the along-fault events that tend to produce amplifications within the basin-structure on the western side of the fault zone.

For the two M_L2.6 repeating events, we compute seismic moment and corner frequency from the earthquake spectra, selecting values that minimize the misfit to the model fit. For each earthquake, we establish a mean and standard deviations from the mean for the full network (N>1000). The values we obtain (fc=11-15Hz, sigma=1.1-1.9MPa) are consistent with similar

past studies (Shearer et al., 2006). We also find the associated uncertainties to be relatively small, exhibiting deviations of 3.2-3.5 Hz for corner frequency and 1.1-1.2 MPa's for stress drop. However, these small uncertainties were only attainable because we have hundreds of measurements for each quake. If instead we assume that any node with variable measurements can contribute to the full range of options, instead we find the range in corner frequency and stress drop increases to 3-20Hz and 0-6Mpa, respectfully. This underscores the importance of not assuming a corner frequency, or stress drop, from a single station can be representative of a broader region, and advocates that multiple measurements from nearby stations be evaluated in aggregate.

Acknowledgements

DATA AND RESOURCES

All data used in this work are available at the IRIS DMC. This work benefited from the Python package ObsPy (Krischer et al., 2015) and Matplotlib for producing colorblind friendly figures (Hunter, 2007).

Appendix A: Removing outliers

In order to properly compare PGV results from different events, we require that the network include at least 1000 nodes, which reduces our dataset to 38 select events. Even with this restriction, the >1000 seismic stations can still contain data from non-optimal nodes that must be removed. A typical approach to remove outliers from a dataset is to compute the mean and standard deviation (sigma) of the data and remove any data that exceeds a threshold of one- or two-sigma from the mean. However, this approach is only appropriate if the data have a normal distribution, which is not necessarily true for our datasets. Given this, instead we use the non-parametric fence test to remove outliers from our data (Rousseeuw and Hubert, 2011). To implement the fence, we first define the interquartile range:

$$iqr = q3-q1 \tag{A1}$$

Next, the fence thresholds are derived using the iqr value and a scale factor:

$$scale = 1.5 \tag{A2}$$
$$fence\_high = q3+iqr*scale \tag{A3}$$
$$fence\_low = q1- iqr*scale \tag{A4}$$

We apply the fence method to the PGV and PGA data separately. We experimented with a scale factor of 3.0, but found 1.5 to be optimal. Using 1.5 as the scale factor retains at least 91% and 86% of the PGV and PGA values, respectively (see supplemental Table S1).

Appendix B: Measuring the skew of the PGV and PGA distributions

The PGV histograms have non-symmetrical distributions, tending to have more higher PGV values than lower values in comparison with the mean. To quantitatively evaluate the extent the PGV distributions differ from a normal distribution we use the skew statistical measure. The Pearson's first skewness coefficient (mode skewness; Doane and Seward, 2011) can be defined as:

$$Skew = (mean - mode)/(sigma) \qquad (B1)$$

Where *mean* is the mean of the full data suite, *mode* is the value corresponding to the peak of the histogram and *sigma* is the standard deviation of the data. Skew values of zero are considered normal distributions, whereas skew values that are positive (negative) have distributions where the right (left) tail is longer than the right (left). For our data we have no negative skew distributions, indicating that if there is a tail in the PGV values the tail will contain higher PGV values. The skew of the PGV and PGA values for each event is computed using the refined data that remains after applying a SNR≥1.5 restriction and implementing the fence (see supplemental Table S1).

Of note, the histograms of the PGV values from a given event typically do not have a normal distribution. We find the skew values range between 0.0 to 1.33 and that all skew values are positive, indicating that all distributions have tails to the right, not tails to the left. We find no correlation between skew and magnitude, depth, distance or back-azimuth. After ruling out these primary factors we turn instead to other local phenomena. The work of Johnson et al., 2019b suggest that ground motions can be generated by the interplay of high winds and surface items coupled to the ground (i.e., trees, building structures, large farm equipment etc.).   We investigated if high winds were strongly contributing to the skewness of our data, but only find a weak dependency between skew and wind velocity. This is understandable as for winds to be a contributor, the seismic wave amplitudes have to be relatively small (<10**-3.5 cm/s), which is smaller than what is typically found in our data.

Tables

Table 1. Select 38 events discussed in this manuscript, time ordered. The mean and standard deviations (σ) were calculated after removing waveforms with SNR≤1.5 and applying a fence to remove outliers (see Appendix A). A full listing that includes all PGV and PGA parameters listed in Table 2 can be found in supplemental Table S1.

Event Time	Magnitude	Lon	Lat	Depth (km)	Distance (km)	Back Azimuth (degree)	PGV mean (cm/s)	PGV σ (cm/s2)
2014-05-1 05:09:48	2.1	-115.43	32.79	13	136.	127	6.30E-05	2.38E-05
2014-05-11 11:47:10	2.2	-115.92	33.05	7.7	83.	131	4.12E-04	1.23E-04
2014-05-11 11:23:35	2.3	-117.72	34.15	10.5	124.	303	2.68E-04	6.09E-05
2014-05-14 08:03:23	2.6	-115.99	33.78	17.1	62.	64	1.51E-03	3.93E-04
2014-05-14 07:45:39	2.6	-115.99	33.77	16.3	61.	65	1.71E-03	4.50E-04
2014-05-13 16:29:22	2.1	-117.68	33.93	8.4	109.	294	2.61E-04	8.63E-05
2014-05-22 08:07:22	2.1	-115.6	33.19	0	99.	113	1.06E-04	2.66E-05
2014-05-22 08:31:11	2.6	-115.24	32.2	9.9	194.	139	4.74E-05	1.38E-05
2014-05-15 12:49:21	2.0	-116.26	32.89	13.1	78.	157	4.83E-04	1.27E-04
2014-05-17 15:19:51	2.2	-116.78	33.34	13.7	28.	218	2.94E-03	6.21E-04
2014-05-24 06:14:05	2.0	-116.85	34.05	16.1	62.	337	7.64E-04	2.00E-04
2014-05-15 09:35:15	2.1	-117	35.08	6	175.	348	4.26E-05	1.21E-05
2014-05-24 23:52:26	2.1	-116.26	33.29	17.1	40.	131	5.41E-04	1.36E-04
2014-05-23 14:14:54	3.1	-115.07	32.35	3.9	193.	132	1.29E-04	3.31E-05
2014-05-23 14:14:57	3.2	-115.18	32.33	11	187.	135	1.29E-04	3.31E-05

2014-05-19 17:07:06	2.2	-116.87	33.83	17.2	41.	321	1.48E-03	3.39E-04
2014-05-18 15:32:30	2.4	-117.27	34.8	8.3	153.	336	2.95E-04	8.49E-05
2014-05-21 11:49:55	2.2	-116.83	34.21	16.3	77.	344	2.12E-04	5.84E-05
2014-05-21 12:49:24	2.2	-116.82	34.25	7.8	82.	345	2.79E-04	7.38E-05
2014-05-26 12:16:07	2.9	-115.72	32.13	4.6	176.	152	1.65E-04	5.19E-05
2014-05-26 12:16:08	2.6	-115.85	32.15	0	168.	156	1.65E-04	5.18E-05
2014-05-26 01:20:05	2.2	-116.6	34.62	7.3	120.	360	1.92E-04	4.86E-05
2014-05-27 02:11:02	2.3	-116.66	33.59	17	8.	311	1.31E-02	3.69E-03
2014-05-28 20:48:02	2.8	-115.25	32.28	13.9	188.	138	6.36E-05	2.20E-05
2014-05-27 19:30:51	3.0	-116.87	34.99	2.8	163.	351	4.97E-04	1.32E-04
2014-05-30 03:00:15	2.2	-117.61	34.16	8.7	117.	307	2.04E-04	5.24E-05
2014-05-31 01:04:34	2.3	-116.61	33.93	16	44.	358	1.62E-03	4.27E-04
2014-05-31 02:59:29	3.8	-118.37	33.59	8.3	164.	273	1.23E-03	3.17E-04
2014-05-19 20:08:52	3.8	-116.82	34.25	7.5	82.	345	1.17E-02	3.16E-03
2014-05-31 10:16:02	2.6	-117.59	35.02	-0.1	189.	331	8.89E-05	2.82E-05
2014-06-01 08:19:25	2.2	-117.82	33.95	14.2	122.	293	1.42E-04	2.95E-05
2014-06-01 13:07:49	2.0	-115.72	32.65	11.4	127.	140	8.02E-05	2.92E-05
2014-06-01 16:29:06	2.6	-116.25	32.9	12.1	77.	156	1.37E-03	3.66E-04
2014-06-02 00:06:21	2.3	-115.99	32.89	11.9	91.	142	4.53E-04	1.56E-04

2014-06-02 00:06:21	2.3	-116.05	32.9	14.2	86.	144	4.62E-04	1.39E-04
2014-06-01 23:44:50	2.1	-115.69	32.57	13.9	136.	142	1.14E-04	2.65E-05
2014-06-02 02:36:43	4.2	-118.49	34.1	4.2	186.	290	5.48E-04	1.27E-04
2014-05-19 22:41:11	2.8	-116.43	34.16	11.8	70.	12	1.21E-03	3.35E-04

Table 2. Key parameters in this work. For each earthquake, we compute and catalogue these values in supplemental Table S1, which is a csv flat file. An asterisk after the parameter name indicates that the value was derived after applying our SNR cut-off and the fence to remove outliers.

Parameter Name	Description
Event time	Earthquake origin time
Mag	Earthquake magnitude
Lon	Earthquake longitude(degrees)
Lat	Earthquake Latitude (degrees)
Depth_km	Earthquake depth (km)
Dist_km	Source station distance (km)
Azi	Source to station azimuth (degrees)
Bazi	Station to source azimuth (degrees)
pgv_min*	Minimum PGV across the network (cm/s)
pgv_max*	Maximum PGV across the network (cm/s)
pgv_mean*	Maximum PGV across the network (cm/s)
pgv_median*	Medium PGV across the network (cm/s)
pgv_std*	Standard deviation of PGV across the network (cm/s)
pga_min*	Minimum PGA across the network (cm/s2)
pga_max*	Maximum PGA across the network (cm/s2)
pga_mean*	Mean PGA across the network (cm/s2)
pga_median*	Median PGA across the network (cm/s2)
pga_std*	Standard deviation of PGA across the network (cm/s2)
n_stats*	Number of stations
fence_mul	Fence scale factor (see equation A1b)
skew_pgv*	Skew of PGV across the network (cm/s)
skew_pga*	Skew of PGA across the network (cm/s2)
%stdofmean_pgv*	PGV: Percentage of the mean that sigma represents (i.e., sigma/mean)
%stdofmean_pga*	PGA: Percentage of the mean that sigma represents (i.e., sigma/mean)
snr_thresh	Signal to noise (SNR) threshold
%fenceV	Percent of stations removed by the fence (PGV)
%fenceA	Percent of stations removed by the fence (PGA)

Supplemental Introduction

This supporting information includes three figures, the first is a companion figure to Figure 3 in the main manuscript showing PGA data instead of PGV data. The second figure is the mapped PGV spatial patterns for the pair of repeating $M_L 2.6$ events on 14 May 2014. This figure highlights the PGV spatial repeatability for similar events. The third figure is similar to Figure 8 in the main manuscript, displaying PGA data instead of PGV data. Table S1 is a csv file that contains a summary of all findings for all 38 events for the parameters listed in Table 2 in the main manuscript.
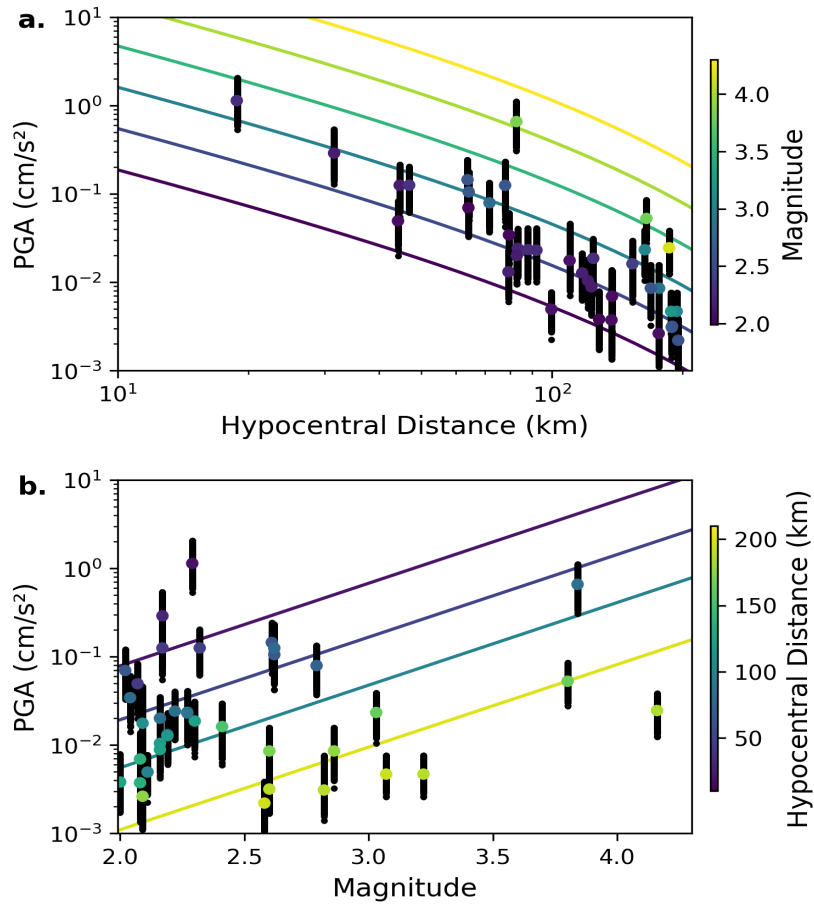
Figure S1. PGA shown as a function of (a) hypocentral distance and (b) magnitude. Colors are as in Figure 3 in the main manuscript.
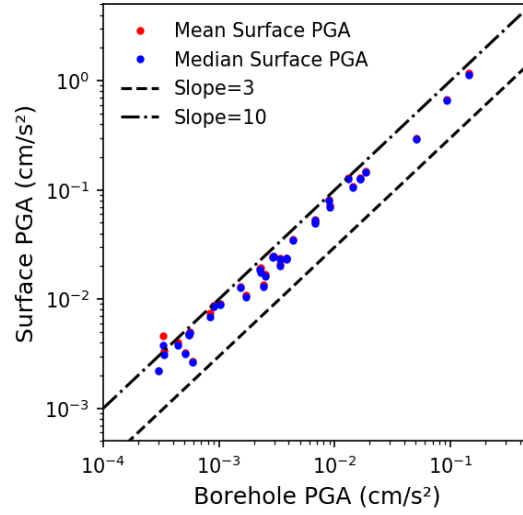
Figure S2. Comparison of borehole and surface measurements, as in Figure 4 in the main manuscript, but for PGA values.
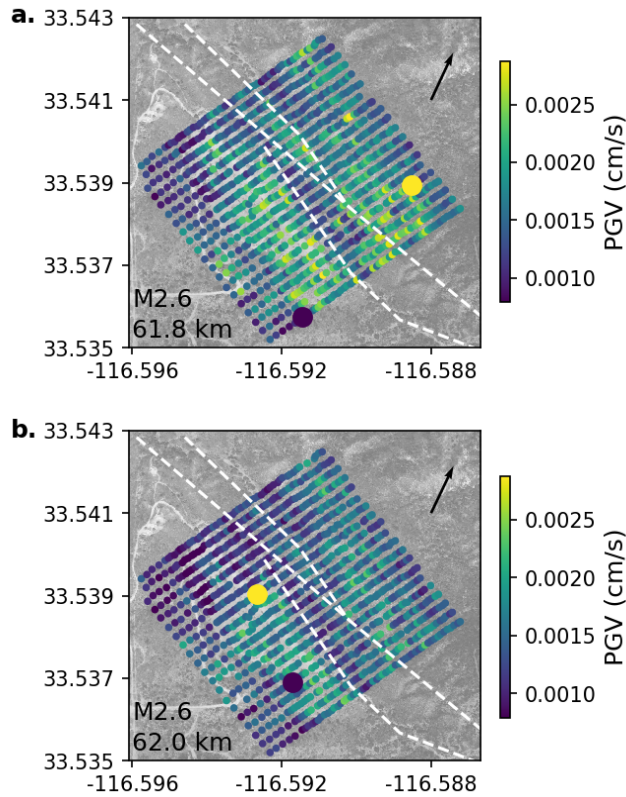
Figure S3. PGV mapped spatial pattern for the pair of repeating $M_L2.6$ events on 14 May 2014 at (**a**) 07:45:39.09 and (**b**) 08:03:22.79. The large dots show the PGV minimum (blue) and maximum (yellow) locations in the array. The black arrow indicates the source back-azimuth. The magnitude and distance are shown in the bottom left. The white dashed lines are the mapped fault traces from the USGS database.

Supplemental Table S1. Listing of the 38 earthquakes in this study and the associated parameters listed in Table 2.

| Event_time	Mag	Lon	Lat	Depth_km	Dist_km	Az	Bazi	pgv_min	pgv_max	pgv_mean	pgv_median	pgv_std	pga_min	pga_max	pga_mean	pga_median	pga_std	n_stats	fenot_mul	skew_pgv	skew_pga	%stdofmean_pgv	%stdofmean_pga	snr_thresh	%kerdv	%kterpA
2014-05-11 15:00:48	2.1	-115.43	32.70	13	136.49	308	127	4.24E-06	1.22E-04	6.02E-05	5.74E-05	1.87E-05	4.40E-04	1.33E-02	6.02E-03	5.71E-03	2.52E-03	1088	1.5	0.87	1.52	31.12	55.3	2	91	87
2014-05-11 11:23:33	2.3	-117.72	34.15	10.5	124.05	303	303	1.08E-06	4.17E-04	1.02E-04	2.28E-04	1.87E-03	4.71E-04	3.11E-02	1.87E-02	1.87E-02	2.52E-03	1088	1.5	0.37	0.28	20.75	22.83	2	99	99
2014-05-11 11:47:10	2.2	-115.92	33.05	7.7	83.02	131	131	1.21E-04	7.27E-04	1.02E-04	3.34E-04	5.46E-04	4.07E-02	5.88E-02	2.42E-02	1.97E-02	4.33E-03	1088	1.5	0.42	0.24	28.01	23.16	2	98	87
2014-05-13 19:29:22	2.1	-117.88	33.93	8.4	109.94	113	294	9.87E-05	4.71E-04	5.46E-04	2.44E-04	4.54E-02	1.94E-02	3.11E-02	2.42E-02	7.30E-03	1088	1.5	0.57	1.3	27.31	37.56	2	91	87
2014-05-14 7:45:39	2.6	-115.99	33.77	16.3	61.75	245	65	8.15E-04	2.87E-03	1.65E-03	4.22E-04	6.42E-02	2.46E-01	1.94E-01	1.49E-01	3.50E-02	1086	1.5	0.39	0.31	24.87	23.53	2	99	99
2014-05-14 8:03:23	2.6	-115.99	33.78	17.1	62.04	245	64	6.79E-04	2.45E-03	1.48E-03	3.43E-04	4.96E-02	1.89E-01	1.10E-01	1.10E-01	2.68E-02	1086	1.5	0.26	0.39	23.14	23.9	2	97	99
2014-05-15 9:35:15	2.1	-117	35.08	6	175.96	188	348	1.73E-05	7.37E-05	4.08E-05	4.83E-03	1.10E-03	2.72E-03	2.64E-03	3.44E-02	1082	1.5	0.34	0.42	26.93	26.95	2	97	95
2014-05-16 12:48:21	2	-116.26	32.89	13.1	78.49	157	157	2.41E-04	1.13E-04	4.91E-04	6.67E-05	6.08E-02	3.55E-02	2.64E-03	3.44E-02	9.20E-03	1082	1.5	0.49	0.52	25.75	23.9	2	99	98
2014-05-17 15:19:51	2.2	-116.78	33.34	13.7	28.38	38	218	1.69E-03	4.39E-03	2.91E-03	5.70E-04	1.42E-01	2.86E-01	8.22E-02	2.77E-01	8.22E-02	1082	1.5	0.14	0.63	19.57	28.55	2	98	96
2014-05-18 15:32:30	2.4	-117.27	34.8	8.3	153.01	156	336	5.08E-04	2.39E-04	2.00E-04	7.82E-05	1.63E-02	4.52E-03	5.24E-03	4.52E-03	1079	1.5	0.27	0.38	26.75	26.82	2	97	97
2014-05-19 17:07:06	2.2	-116.87	33.83	17.2	41.12	321	321	6.94E-04	2.25E-03	1.45E-03	3.21E-04	1.66E-01	1.26E-01	1.29E-02	1.87E-02	1.87E-01	1079	1.5	0.56	0.50	21.89	25.75	2	98	98
2014-05-19 20:05:52	3.8	-116.87	34.25	7.5	82.48	166	345	4.88E-03	1.68E-02	1.18E-02	6.74E-01	6.06E-01	1.96E+00	6.06E-01	1.94E-01	1042	1.5	0.45	0.34	24.02	25.93	2	97	97
2014-05-19 22:41:11	2.8	-116.43	34.16	11.8	70.83	192	12	5.46E-04	2.16E-03	1.37E-03	3.20E-04	3.70E-02	7.94E-02	6.94E-02	7.94E-02	1.94E-02	1002	1.5	0.46	0.41	26.45	23.87	2	97	97
2014-05-21 11:46:55	2.2	-116.83	34.21	16.3	77.72	194	344	9.13E-05	3.56E-04	2.02E-04	5.23E-05	6.03E-03	2.28E-02	1.31E-02	3.20E-03	2.05E-03	1079	1.5	0.5	0.5	25.16	23.69	2	97	99
2014-05-21 12:49:24	2.2	-116.82	34.25	7.8	82.6	165	345	1.19E-04	4.82E-04	2.70E-04	6.67E-05	9.47E-03	2.06E-02	2.02E-02	5.07E-03	0.44	1079	1.5	0.34	0.44	24.2	24.35	2	98	97
2014-05-22 8:07:22	2.1	-115.6	33.19	0	99.69	203	113	5.20E-05	1.04E-04	1.02E-04	2.30E-05	7.74E-03	5.00E-03	4.54E-03	9.72E-04	5.07E-03	1085	1.5	0.29	0.29	22.17	19.47	2	96	98
2014-05-22 8:31:11	2.6	-115.24	32.2	9.9	194.98	320	139	8.31E-05	1.06E-04	1.27E-05	3.84E-03	2.23E-03	5.07E-03	5.57E-04	0.38	1085	1.5	0.55	0.38	27.15	24.93	2	97	95
2014-05-23 14:14:54	3.1	-115.07	32.35	3.9	193.73	313	132	5.97E-05	2.00E-04	1.24E-04	7.60E-03	4.81E-03	9.76E-04	4.69E-03	0.52	1079	1.5	0.52	0.52	22.65	20.29	2	96	95
2014-05-24 14:06	3.2	-115.18	32.33	11	187.78	316	135	5.97E-05	2.00E-04	1.24E-04	2.85E-05	7.60E-03	4.69E-03	4.69E-03	0.53	1082	1.5	0.38	0.53	22.64	20.29	2	96	95
2014-05-24 23:52:20	2	-116.85	34.05	16.1	62.15	157	337	3.25E-04	1.31E-03	7.61E-04	1.89E-04	2.28E-02	7.18E-02	6.98E-02	1.79E-02	0.43	1082	1.5	0.38	0.43	24.79	24.55	2	98	98
2014-05-31 1:20:05	2.1	-116.6	33.29	17.1	40.82	311	311	2.77E-04	8.92E-04	5.37E-04	1.24E-04	1.08E-02	5.09E-02	4.95E-02	1.17E-02	0.42	1079	1.5	0.44	0.42	24.14	22.97	2	97	97
2014-05-31 10:16:02	2.2	-116.6	34.02	7.3	120.78	180	360	3.36E-05	3.23E-04	1.88E-04	4.62E-05	1.82E-02	1.04E-02	3.17E-03	2.58E-02	0.52	1070	1.5	0.38	0.52	23.73	23.78	2	98	98
2014-06-01 8:16:29	2.9	-115.72	32.13	4.6	176.38	333	152	6.54E-05	3.07E-04	1.64E-04	5.08E-05	3.21E-03	8.66E-03	8.56E-03	2.43E-03	0.36	1070	1.5	0.36	0.36	30.81	28.1	2	99	100
2014-06-01 16:10:08	2.6	-115.85	32.15	0	168.94	386	156	6.54E-05	3.07E-04	1.64E-04	5.08E-05	3.21E-03	8.66E-03	8.56E-03	2.43E-03	0.36	1070	1.5	0.36	0.36	30.74	28.1	2	98	100
2014-05-27 2:11:02	2.3	-116.66	33.59	17	8.13	131	311	6.17E-03	2.23E-02	1.26E-02	3.23E-03	5.31E-01	2.16E+00	1.19E+00	3.36E-01	0.5	1069	1.5	0.45	0.5	24.73	27.46	2	98	98
2014-05-27 19:30:51	3	-116.67	34.99	2.8	163.62	351	351	8.50E-04	1.25E-04	2.37E-02	2.37E-02	5.53E-03	0.34	1067	1.5	0.34	0.34	25.23	23.29	2	98	98
2014-05-28 20:40:02	2.8	-115.25	32.28	13.9	188.16	319	138	1.30E-05	1.19E-04	5.90E-05	1.79E-05	1.93E-03	8.13E-03	3.08E-03	1.29E-03	1.43	1067	1.5	0.69	1.43	29.07	38.04	2	92	86
2014-05-30 3:00:16	2.2	-117.01	34.16	8.7	117.06	128	307	1.04E-04	2.04E-04	2.00E-04	4.85E-05	6.25E-03	2.12E-02	1.30E-02	2.84E-03	0.31	1057	1.5	0.31	0.31	23.76	21.89	2	98	98
2014-05-31 1:04:34	2.3	-116.61	33.03	16	44.09	179	358	6.97E-04	2.62E-03	1.61E-03	3.74E-04	1.32E-01	2.99E-02	1.14E-02	0.28	1048	1.5	0.31	0.28	23.03	22.37	2	98	96
2014-05-31 2:39:29	3.8	-116.37	33.59	8.3	164.8	92	273	5.62E-04	2.05E-03	1.21E-03	2.87E-04	8.53E-02	1.30E-02	5.38E-02	0.35	1044	1.5	0.37	0.35	23.48	21.24	2	98	98
2014-05-31 10:16:02	2.6	-117.59	35.02	-0.1	189.11	151	331	3.33E-05	8.07E-05	1.07E-05	2.37E-05	3.25E-03	1.71E-03	0.46	1040	1.5	0.41	0.46	27.3	24.82	2	97	98
2014-06-01 8:10:25	2.2	-117.82	33.95	14.2	122.44	112	293	8.00E-05	2.20E-04	1.40E-04	2.77E-05	4.19E-03	9.02E-03	2.07E-03	0.37	1018	1.5	0.37	0.37	19.6	22.91	2	97	97
2014-06-01 13:07:49	2	-115.72	32.65	7.5	127.94	140	321	1.66E-05	1.46E-04	7.87E-05	2.41E-05	8.24E-03	3.85E-03	1.30E-02	0.35	1014	1.5	0.35	0.35	30.68	32.2	2	96	98
2014-06-01 16:29:06	2.6	-116.26	32.9	12.1	77.09	156	156	5.54E-04	2.29E-03	1.37E-03	3.46E-04	4.20E-02	1.30E-01	7.44E-03	3.78E-02	0.46	1013	1.5	0.16	0.46	25.22	28.76	2	99	98
2014-04-01 23:44:50	2.1	-115.69	32.57	13.9	136.84	142	142	5.70E-05	1.74E-04	1.05E-04	2.22E-05	3.52E-03	1.32E-02	6.69E-03	2.00E-03	0.78	1008	1.5	0.32	0.78	19.87	26.94	2	99	94
2014-06-02 0:06:21	2.3	-115.99	32.89	11.9	91.28	322	142	1.81E-04	8.51E-04	4.34E-04	1.39E-04	4.41E-02	2.39E-02	2.32E-02	7.01E-03	0.4	1009	1.5	0.36	0.4	30.9	29.46	2	97	98
2014-06-02 0:08:21	2.3	-116.05	32.9	14.2	86.88	324	142	1.81E-04	8.13E-04	4.06E-04	1.39E-04	4.10E-02	2.39E-02	2.35E-02	6.23E-03	0.31	1009	1.5	0.31	0.31	27.85	26.17	2	97	97
2014-06-02 2:36:43	4.2	-116.49	34.1	4.2	186.13	109	290	2.83E-04	8.65E-04	5.49E-04	5.35E-04	1.14E-04	3.82E-02	2.46E-02	2.35E-02	6.23E-03	0.17	1004	1.5	0.35	0.17	21	19.82	2	98	98

REFERENCES

Abercrombie, R. E. (1995). Earthquake source scaling relationships from -1 to 5 ML, using seismograms recorded at 2.5 km depth, *J. Geophys. Res.,* 100, 24015-24036.

Abercrombie, R., & Leary, P. (1993). Source parameters of small earthquakes recorded at 2.5 km depth, Cajon Pass, southern California: implications for earthquake scaling. *Geophysical Research Letters*, *20*(14), 1511-1514.

Aki, K., and P. G. Richards (2002). Quantitative Seismology (second ed.), University Science Books, Sausalito, California.

Ammon, C. J., Lay, T., Kanamori, H., & Cleveland, M. (2011). A rupture model of the 2011 off the Pacific coast of Tohoku Earthquake. *Earth, Planets and Space,* 63(7), 693-696.

Anderson, J. G. (1986). Implication of attenuation for studies of the earthquake source, Earthquake Source Mechanics, Geophysical Monograph 37, (Maurice Ewing Series 6), American Geophysical Union, Washington, D.C., 311-318.

Anderson, J. G. (2007). Physical processes that control strong ground motion, In Hiroo Kanamori, Volume Editor; Gerald Schubert, Editor in Chief (Ed.), Treatise on Geophysics, Volume 4, Earthquake Seismology (vol. 4, pp. 513-565). Amsterdam: Elsevier.

Atkinson, Gail M., and David J. Wald. "Did You Feel It?" intensity data: A surprisingly good measure of earthquake ground motion." *Seismological Research Letters* 78.3 (2007): 362-368.

Baltay, A. S. and J. Boatwright (2015), Ground-motion observations of the 2014 South Napa Earthquake, *Seism. Res. Lett.,* 86(2A), doi: 10.1785/0220140232.

Baltay, A. S. and T. C. Hanks (2014), Understanding the magnitude dependence of PGA and PGV in NGA-West2 Data, *Bull. Seis. Soc. Am.,* 104(6), doi: 10.1785/0120130283.

Baltay, A. S., Hanks, T. C., & Beroza, G. C. (2013). Stable stress-drop measurements and their variability: Implications for ground-motion prediction. *Bull. Seism. Soc. Am., 103*(1), 211-222.

Baltay, A.S., T. C. Hanks and N. A. Abrahamson (2017). Uncertainty, Variability, and Earthquake Physics in GMPEs, *Bull. Seism. Soc. Am.,* doi: 10.1785/0120160164.

Ben-Zion, Y., Vernon, F. L., Ozakin, Y., Zigone, D., Ross, Z. E., Meng, H., ... & Barklage, M. (2015). Basic data features and results from a spatially dense seismic array on the San Jacinto fault zone. *Geophysical Journal International,* 202(1), 370-380.

Beresnev, I. A. (2001). What we can and cannot learn about earthquake sources from the spectra of seismic waves. *Bull. Seism. Soc. Am., 91*, 397-400.

Berger, J., L. M. Baker, J. N. Brune, J. B. Fletcher, T. C. Hands, and F. L. Vernon (1984). The Anza array: a high-dynamic-range, broad-band, digitally-radiotelemetered, seismic array, *Bull. Seism. Soc. Am.,* 89, 1469-1481.

Bommer, J. J., & Abrahamson, N. A. (2006). Why do modern probabilistic seismic-hazard analyses often lead to increased hazard estimates?. *Bull. Seism. Soc. Am.,* 96(6), 1967-1977.

Bostock, M. G., Thomas, A. M., Rubin, A. M., & Christensen, N. I. (2017). On corner frequencies, attenuation, and low-frequency earthquakes. *J. of Geophysical Research: Solid Earth,* 122(1), 543-557.

Brune, J. N. (1970). Tectonic stress and the spectra of seismic shear waves from earthquakes. *J. of Geophysical Research,* 75(26), 4997-5009.

Brune, J. N. (1971). Correction to tectonic stress and the spectra of seismic shear waves from earthquakes. *J. geophys. Res,* 76(20), 5002.

Denolle, M. A., Dunham, E. M., Prieto, G. A., & Beroza, G. C. (2014). Strong ground motion prediction using virtual earthquakes. *Science,* 343(6169), 399-403.

Doane, D. P., & Seward, L. E. (2011). Measuring skewness: a forgotten statistic?. *Journal of Statistics Education*, *19*.

Farrell, J., Wu, S. M., Ward, K. M., & Lin, F. C. (2018). Persistent noise signal in the FairfieldNodal three-component 5-Hz geophones. *Seismological Research Letters*, *89*, 1609-1617.

Field, E. H., Jordan, T. H., Page, M. T., Milner, K. R., Shaw, B. E., Dawson, T. E., ... & Weldon, R. J. (2017). A synoptic view of the third uniform California earthquake rupture forecast (UCERF3). *Seismological Research Letters,* 88, 1259-1267.

Gallovič, F. (2016). Azimuthal Dependence of the Ground Motion Variability from Scenario Modeling of the 2014 Mw6. 0 South Napa, California, Earthquake Using an Advanced Kinematic Source Model. *Pure and Applied Geophysics,* 1-12.

Ghofrani, H., Atkinson, G. M., Schultz, R., & Assatourians, K. (2019). Short-term hindcasts of seismic hazard in the western Canada sedimentary basin caused by induced and natural earthquakes. *Seismological Research Letters*, *90*, 1420-1435.

Goebel, T. H. W., Hauksson, E., Plesch, A., & Shaw, J. H. (2018). Detecting significant stress drop variations in large micro-earthquake datasets: A comparison between a convergent step-over in the San Andreas Fault and the Ventura thrust fault system, Southern California. In *Earthquakes and Multi-hazards Around the Pacific Rim, Vol. I*(pp. 117-136). Birkhäuser, Cham.

Graves, R., Jordan, T. H., Callaghan, S., Deelman, E., Field, E., Juve, G., ... & Okaya, D. (2011). CyberShake: a physics-based seismic hazard model for Southern California. *Pure and Applied Geophysics,* 168(3-4), 367-381.

Hanks, T. C., & McGuire, R. K. (1981). The character of high-frequency strong ground motion. *Bull. Seismol. Soc. Am.,* 71(6), 2071-2095.

Hanks, TC (1975). Strong ground motion of the San Fernando, California, earthquake: ground displacements, *Bull. Seismol. Soc. Am.,* 65 (1), 193-225

Hauksson, E. (1990). Earthquakes, faulting, and stress in the Los Angeles basin. Journal of Geophysical Research: Solid Earth, 95(B10), 15365-15394.

Hauksson, E. (2015). Average stress drops of Southern California earthquakes in the context of crustal geophysics: implications for fault zone healing, *Pure and Applied Geophysics,* 1359-1370.

Hillers, G., & Campillo, M. (2016). Fault zone reverberations from cross-correlations of earthquake waveforms and seismic noise. *Geophysical Journal International,* 204(3), 1503-1517.

Hiramatsu, Y., Yamanaka, H., Tadokoro, K., Nishigami, K. Y., & Ohmi, S. (2002). Scaling law between corner frequency and seismic moment of microearthquakes: Is the breakdown of the cube law a nature of earthquakes?. *Geophysical Research Letters*, *29*, 52-1.

Hough, S. E., J. G. Anderson, J. Brune, F. L. Vernon, J. Berger, J. Fletcher, L. Haar, T. Hanks, and L. Baker (1988). Attenuation near Anza, California, *Bull. Seismol. Soc. Am.,* 78, 672-691.

Huang, Y., Beroza, G. C., & Ellsworth, W. L. (2016). Stress drop estimates of potentially induced earthquakes in the Guy-Greenbrier sequence. *J. of Geophysical Research: Solid Earth*, *121*(9), 6597-6607.

Hunter, J. D. (2007). Matplotlib: A 2D graphics environment. *Computing in science & engineering*, *9*(3), 90.

Ide, S., & Beroza, G. C. (2001). Does apparent stress vary with earthquake size?. *Geophysical Research Letters*, *28*(17), 3349-3352.

Johnson, C. W., Vernon, F., Nakata, N., & Ben-Zion, Y. (2019a). Atmospheric Processes Modulating Noise in Fairfield Nodal 5 Hz Geophones. *Seismological Research Letters*. doi:10.1785/0220180383.

Johnson, C.W., H. Meng, F.L. Vernon, and Y. Ben-Zion (2019b) Characteristics of ground motion generated by interaction of wind gusts with trees, structures and other obstacles above the surface. Journal of Geophysical Research: Solid Earth, 124. doi:10.1029/2018jb017151

Kilb, D. G Biasi, J Anderson, J Brune, Z Peng, FL Vernon (2012). A comparison of spectral parameter kappa from small and moderate earthquakes using southern California ANZA seismic network data, *Bull. Seismol. Soc. Am.,* 102, 284-300.

Kilb, D., Gomberg, J., & Bodin, P. (2000). Triggering of earthquake aftershocks by dynamic stresses. *Nature,* 408(6812), 570-574.

King, C. Y., & Knopoff, L. (1968). Stress drop in earthquakes. *Bull. Seismol. Soc. Am.,* 58(1), 249-257.

Klimasewski, A., Sahakian, V., Baltay, A., Boatwright, J., Fletcher, J. B., & Baker, L. M. (2019). κ0 and Broadband Site Spectra in Southern California from Source Model-Constrained Inversion. Bull. Seismol. Soc. Am., (in press).

Kurzon, I., Vernon, F. L., Ben-Zion, Y., & Atkinson, G. (2014). Ground Motion Prediction Equations in the San Jacinto Fault Zone: Significant Effects of Rupture Directivity and Fault Zone Amplification. *Pure and Applied Geophysics,* 171(11), 3045-3081.

Krischer, L., Megies, T., Barsch, R., Beyreuther, M., Lecocq, T., Caudron, C., & Wassermann, J. (2015). ObsPy: A bridge for seismology into the scientific Python ecosystem. *Computational Science & Discovery*, 8(1), 014003.

Lee, En-Jui, and Po Chen (2016). Improved Basin Structures in Southern California Obtained Through Full-3D Seismic Waveform Tomography (F3DT). *Seismological Research Letters*.

Lewis, M. A., Peng, Z., Ben-Zion, Y., & Vernon, F. L. (2005). Shallow seismic trapping structure in the San Jacinto fault zone near Anza, California. *Geophysical Journal International,* 162(3), 867-881.

Li, Y. G., & Vernon, F. L. (2001). Characterization of the San Jacinto fault zone near Anza, California, by fault zone trapped waves. *J. of Geophysical Research: Solid Earth,* 106(B12), 30671-30688.

Lin, P. S., Chiou, B., Abrahamson, N., Walling, M., Lee, C. T., & Cheng, C. T. (2011). Repeatable source, site, and path effects on the standard deviation for empirical ground-motion prediction models. *Bull. Seismol. Soc. Am.,* 101(5), 2281-2295.

Lindsey, E. O., and Y. Fialko (2016), Geodetic constraints on frictional properties and earthquake hazard in the Imperial Valley, Southern California, *J. Geophys. Res. Solid Earth,* 121, 1097–1113, doi:10.1002/2015JB012516.

McNamara, D. E., Gee, L., Benz, H. M., & Chapman, M. (2014). Frequency-dependent seismic attenuation in the eastern United States as observed from the 2011 central Virginia earthquake and aftershock sequence. *Bull. Seismol. Soc. Am., 104*(1), 55-72.

Pesaresi, D., & Horn, N. (2004). Data integration from the scientific community and CTBTO: the Italian NDC experience with Antelope. *Seismological Research Letters,* 75(3), 379-384.

Press, F. (1964). Seismic wave attenuation in the crust, *J. of Geophys. Res.,* 69, 4417-4418, DOI: 10.1029/JZ069i020p04417.

Qiu, H., Ben-Zion, Y., Ross, Z. E., Share, P. E., & Vernon, F. L. (2017). Internal structure of the San Jacinto fault zone at Jackass Flat from data recorded by a dense linear array. *Geophysical Journal International*, *209*(3), 1369-1388.

Ross, Z. E., Meier, M. A., & Hauksson, E. (2018). P wave arrival picking and first-motion polarity determination with deep learning. *J. of Geophys. Res., 123*, 5120-5129.

Rousseeuw, P. J., & Hubert, M. (2011). Robust statistics for outlier detection. Wiley Interdisciplinary Reviews: Data Mining and Knowledge Discovery, 1(1), 73-79.

Roux, P., Moreau, L., Lecointre, A., Hillers, G., Campillo, M., Ben-Zion, Y., ... & Vernon, F. (2016). A methodological approach towards high-resolution surface wave imaging of the San Jacinto Fault Zone using ambient-noise recordings at a spatially dense array. *Geophysical Journal International,* 206(2), 980-992.

Sahakian, V. J., Baltay, A., Hanks, T. C., Buehler, J., Vernon, F. L., Kilb, D., & Abrahamson, N. A. (2019). Ground Motion Residuals, Path Effects, and Crustal Properties: A Pilot Study in Southern California. *J. of Geophysical Research*, *124*, 5738-5753.

Sahakian, V., Baltay, A., Hanks, T., Buehler, J., Vernon, F., Kilb, D., & Abrahamson, N. (2018). Decomposing Leftovers: Event, Path, and Site Residuals for a Small-Magnitude Anza Region GMPEDecomposing Leftovers: Event, Path, and Site Residuals for a Small-Magnitude Anza Region GMPE. *Bull. Seismol. Soc. Am., 108*, 2478-2492.

SCEC, Putting Down Roots in Earthquake country (2011), an online handbook, http://www.earthquakecountry.org/roots/socal-costs.html

Share, P. E., Ben-Zion, Y., Ross, Z. E., Qiu, H., & Vernon, F. L. (2017). Internal structure of the San Jacinto fault zone at Blackburn Saddle from seismic data of a linear array. *Geophysical Journal International*, *210*(2), 819-832.

Shearer, P. M., G. A. Prieto, and E. Hauksson (2006). Comprehensive analysis of earthquake source spectra in southern California, *J. Geophys. Res.* 111, B06303, doi 10.1029/2005JB003979.

Stewart, J. P., Boore, D. M., Seyhan, E., & Atkinson, G. M. (2016). NGA-West2 equations for predicting vertical-component PGA, PGV, and 5%-damped PSA from shallow crustal earthquakes. *Earthquake Spectra,* 32(2), 1005-1031.

Thompson E. M. and D.J. Wald, (2016). "Uncertainty in VS30-Based Site Response", *Bull. Seismol. Soc. Am.,* doi: 10.1785/0120150214.

Villani, M., & Abrahamson, N. A. (2015). Repeatable site and path effects on the ground-motion sigma based on empirical data from southern California and simulated waveforms from the CyberShake platform. *Bull. Seismol. Soc. Am., 105*(5), 2681-2695.

Wang, J. H. (2019). A Review on Scaling of Earthquake Source Spectra. *Surveys in Geophysics*, *40*, 133-166.

Wessel, P., & Smith, W. H. (1991). Free software helps map and display data. Eos, Transactions American Geophysical Union, 72(41), 441-446.

Yabe, S., Baltay, A. S., Ide, S., & Beroza, G. C. (2014). Seismic-wave attenuation determined from tectonic tremor in multiple subduction zones. *Bull. Seismol. Soc. Am., 104*(4), 2043-2059.

Yoshimitsu, N., Ellsworth, W. L., & Beroza, G. C. (2019). Robust Stress Drop Estimates of Potentially Induced Earthquakes in Oklahoma: Evaluation of Empirical Green's Function. *Journal of Geophysical Research: Solid Earth* (in press).

Zigone, D., Ben-Zion, Y., Campillo, M., & Roux, P. (2015). Seismic tomography of the Southern California plate boundary region from noise-based Rayleigh and Love waves. *Pure and Applied Geophysics,* 172(5), 1007-1032.

Zöller, G., & Ben-Zion, Y. (2014). Large earthquake hazard of the San Jacinto fault zone, CA, from long record of simulated seismicity assimilating the available instrumental and paleoseismic data. *Pure and Applied Geophysics,* 171(11), 2955-2965.